ASME Journal of Electrochemical Energy Conversion and Storage
Online journal at:
https://asmedigitalcollection.asme.org/electrochemical

Daniel Juarez Robles[1]
Mem. ASME
Battery System Research and Innovation,
Southwest Research Institute,
6220 Culebra Road,
San Antonio, TX 78238
e-mail: daniel.juarezrobles@swri.org

Swapnil S. Salvi
Mem. ASME
Battery System Research and Innovation,
Southwest Research Institute,
6220 Culebra Road,
San Antonio, TX 78238
e-mail: swapnil.salvi@swri.org

Andre Swarts
Mem. ASME
Battery System Research and Innovation,
Southwest Research Institute,
6220 Culebra Road,
San Antonio, TX 78238
e-mail: andre.swarts@swri.org

Jayant V. Sarlashkar
Mem. ASME
Powertrain Engineering,
Southwest Research Institute,
6220 Culebra Road,
San Antonio, TX 78238
e-mail: jayant.sarlashkar@swri.org

The Effect of Immersion Cooling on Lithium Plating Degradation in Lithium-Ion Batteries

The objective of this study is to investigate the interaction between immersion cooling and lithium plating as a degradation mechanism in high charge rate Li-ion batteries. Commercial 5 Ah cylindrical cells (graphite/lithium nickel manganese cobalt oxide (NMC)) were subjected to aggressive charge cycling (1.3C) under different thermal boundary conditions: air cooling (reference) and immersion liquid cooling with flowrates between 0 and 4 lpm. The reference cell aged in air was confirmed to have significant lithium plating by performing a destructive physical analysis and subsequent electrode analysis. The plated cell validated the characteristic impedance drop signature, in the high state of charge (SOC) region, on the transition impedance obtained via pseudo-electrochemical impedance spectroscopy (EIS). The signature was then used as a nondestructive diagnostic for plating in the immersion-cooled cells. Counterintuitively, the immersion-cooled cells, particularly those with higher coolant flowrates, exhibited faster capacity fade, higher internal resistance, and higher transition impedance after only 70 equivalent cycles compared to the air-cooled cells. Pseudo-EIS corroborated this, showing a more pronounced impedance drop at high SOC (signature of lithium plating) in the cells cooled with higher flowrates. This suggested that, while immersion cooling effectively reduced bulk temperature, the intensive cooling at high flowrates lowered the cell's operating temperature, thereby increasing internal resistance and overpotential. This drove the anode potential below 0.0 V versus Li/Li$^+$, promoting lithium plating and degradation and highlighting the need for dynamic thermal management strategies during fast charging, especially in conjunction with effective thermal management capabilities such as immersion cooling.
[DOI: 10.1115/1.4070548]

Keywords: batteries, electrochemical storage, reliability, durability, and damage tolerance, thermal management

Introduction

Background. Lithium-ion batteries (LIBs) are essential components for powering modern applications, including portable electronics, electric vehicles, and grid-scale energy storage systems. Optimizing their performance, safety, and longevity requires a deep understanding and precise control of their operating conditions and internal electrochemical responses, as lifespan is highly susceptible to these factors. Temperature is one of the key operating conditions in LIB life and safety, where both extremely low and high temperatures can significantly accelerate degradation mechanisms, such as lithium plating. Even more, the need for faster charging rates turns into thermal management challenges, leading to higher cell temperatures. While new thermal management solutions like immersion cooling have proven effective at nominal operating rates, their specific influence on high-rate performance and the resulting implications for mitigating lithium plating formation remains critical and sometimes unclear.

Degradation Mechanisms. The capacity of LIBs to store energy depletes over time. Battery ageing along with capacity loss is a consequence of cycling, storage, and handling conditions. From all three factors, calendar ageing and cycle ageing are the ones dominating cell life. Calendar ageing refers to the capacity loss that occurs when the cell is on the shelf and not in use. However, cycle ageing refers to capacity fade and degradation of a cell being used continuously. It is dependent on the working conditions under which a battery is being used. High charge and discharge rates, high and low ambient temperatures, operating voltage, and number of cycles are the major parameters decreasing the cell life and aggravating the battery ageing phenomenon [1,2].

Cell ageing causes degradation of the battery components including electrodes, electrolyte, separator, and current collectors. Degradation mechanisms include loss of active material on the cathode and anode, and loss of lithium inventory [3]. Formation of solid electrolyte interphase (SEI) due to the reaction of the electrolyte with the anode is an unavoidable degradation mechanism that consumes active lithium. Under extreme conditions, such as very low temperature or high charge rates, lithium may deposit on the anode surface instead of intercalating. This phenomenon is commonly known as lithium plating. Lithium deposition

[1]Corresponding author.
Manuscript received October 14, 2025; final manuscript received November 25, 2025; published online December 18, 2025. Assoc. Editor: Feng Hao.

happens when the potential of graphite falls below 0.0 V versus Li/Li^+, hindering lithium intercalation into the graphite solid phase [4]. The plated lithium reacts with the electrolyte forming a new SEI layer and can detach from the plated lithium, turning into electrochemically dead lithium [5]. Attia et al. studied the nonlinear ageing behavior after prolonged cycling of LIBs at moderate temperature and charging rates. They evaluated different approaches to detect the "knee" point where the change from linear to nonlinear degradation happens and is assumed to be the point where lithium plating becomes the dominant degradation process [6]. The consequences of lithium plating are multifaceted. First, the irreversible consumption of cyclable lithium reduces capacity and shortens cell life. Second, the metallic lithium is prone to forming mossy or dendritic morphologies, which can puncture the separator and trigger internal short circuits, potentially leading to thermal runaway. Third, lithium plating alters the interfacial chemistry of the anode by promoting side reactions with the electrolyte, accelerating SEI growth and resistance increase. For all those reasons, detection of lithium plating during normal battery operation has become a central research focus in the battery technology industry.

A broad range of detection strategies has been explored, spanning electrochemical, physical, and material–analytical approaches. These methods can be broadly categorized as ex situ destructive techniques and in situ or operando nondestructive techniques. Ex situ techniques, such as postmortem scanning electron microscopy, Raman spectroscopy, or optical imaging, provide direct confirmation of plated lithium but necessarily destroy the cell, making them impractical for routine diagnostics. In contrast, operando detection methods seek to identify indirect electrochemical or physical signatures of lithium plating during cycling, enabling continuous monitoring and potential integration into battery management systems (BMS). One of the journal reviews emphasized the urgent need for both mechanistic understanding and reliable detection strategies for anode lithium plating [7]. It highlighted the adverse effects of lithium plating on performance and safety and summarized in situ and ex situ characterization approaches, while also highlighting the operational conditions that exacerbate plating. Another comprehensive review focused on detection methods, identifying knowledge gaps in accurately establishing lithium plating boundaries [8]. They stressed the need for coupling experimental observations with modeling and advanced analysis techniques to define safe operating windows, especially under fast-charging conditions where the plating risk is most severe.

Electrochemical signatures remain one of the most widely studied indicators of lithium plating. For example, Petzl and Danzer introduced a nondestructive method based on identifying a voltage plateau during discharge, corresponding to the stripping of plated lithium [9]. This provided a way to not only detect but also quantify lithium plating, while distinguishing between reversible and irreversible fractions. Burns et al. used high precision coulometry, showing that minute losses in coulombic efficiency during cycling could reveal the onset of plating [10]. Such methods demonstrated high sensitivity but required precision instruments that may not be practical in all operating environments.

Impedance-based approaches have gained significant attention due to their ability to probe interfacial processes without disassembling the cell. Chen et al. demonstrated the utility of the distribution of relaxation time analysis in identifying characteristic frequency shifts associated with plating [11]. Similarly, Koseoglou et al. employed dynamic electrochemical impedance spectroscopy (EIS) to detect plating in real time by superimposing sinusoidal perturbations during charging [12]. They showed that lithium plating decreases the interfacial impedance, a phenomenon that could be tracked online. Straβer et al. further refined impedance-based diagnostics by proposing an operando EIS method that monitored changes in the real part of impedance across the state of charge (SOC) to identify plating onset [13]. Importantly, this work demonstrated integration of EIS-based diagnostics into automotive-relevant setups, addressing concerns about measurement overhead. The push toward practical, real-time diagnostics has intensified in recent years, particularly with the growing adoption of fast charging. Zhang et al. proposed an elegant approach exploiting transient reductions during charging internal resistance due to lithium re-intercalation, enabling online plating detection with only voltage and current signals [14]. The method achieved 100% accuracy under diverse charging conditions and required no additional hardware, highlighting its applicability for BMS integration. Shen et al. took a complementary approach by combining dynamic impedance signatures with machine learning, using long short-term memory models to achieve highly accurate online detection of plating onset during constant and multistage fast-charging protocols [15]. Their method achieved errors below 2.5% SOC and was validated across multiple chemistries and temperatures. Such studies demonstrate a clear trend toward leveraging impedance-derived features, adaptive algorithms, and low-overhead signals for practical deployment.

The pseudo-EIS method proposed by Koleti used intermittent current pulses during battery charging to mimic a full EIS test [16]. The objective was to capture the transition from charge transfer to diffusion, a key phenomenon visible as a "knee" on the EIS Nyquist plot. The transition point is defined by the transition frequency (f_{TR}), which marks the intersection between the charge transfer semicircle and the diffusion tail commonly represented by the Warburg impedance. It had been observed that this frequency and the corresponding transition impedance (Z_{TR}) have a strong dependence on the state of charge. Once the f_{TR} was identified, it was used to calculate a reference time (t_{ref}) for diffusion, which is equal to $1/f_{TR}$. Our calculated reference time was about 3 s, aligning with findings from previous studies and confirming that this duration is sufficient for both processes to occur [16,17]. The core difference between EIS and pseudo-EIS lies in how they handle impedance. Regular EIS linearizes the battery's behavior, meaning it assumes impedance is constant regardless of the applied current. Pseudo-EIS, however, specifically detects the nonlinearity of impedance, observing how it changes with different current pulse magnitudes (both low and high C-rates). This is crucial because lithium plating can be inferred if the high C-rate impedance is lower than its low C-rate counterpart. In a sense, the high charge rate leads to a diffusion-limited condition, but the low charge rate does not. While regular EIS can infer SOH changes by comparing current data to early-life data, pseudo-EIS provides a more immediate assessment. It can determine SOH by comparing low C-rate and high C-rate impedances within the same test, eliminating the need for historical data.

Beyond electrochemical methods, researchers have also explored mechanical and acoustic signatures of lithium plating. Huang et al. and Zhu et al. developed pressure-based diagnostics, observing that the derivative of cell pressure with respect to charge (dP/dQ) revealed distinct features when lithium plating occurred [18,19]. Their work demonstrated that differential pressure sensing could not only detect plating but also serve as feedback for adaptive charging protocols, enabling mitigation in real time. Similarly, Xu et al. explored ultrasonic time of flight as detection metric, showing high sensitivity to internal structural changes caused by lithium deposition [20]. Such approaches offer strong potential for onboard monitoring, given their nondestructive nature and relatively straightforward integration into cell modules. Optical and destructive validation methods remain critical for benchmarking. Ringbeck et al. compared electrical and optical methods, showing consistent agreement between electrochemical signatures of plating and microscopic evidence of dendritic structures on anodes [21]. This type of validation has become a standard practice in the community to establish confidence in nondestructive detection techniques.

While much of the literature emphasizes electrochemical or mechanical detection methods, relatively few studies explicitly consider thermal management as a variable in lithium plating behavior. Liu et al. addressed this gap by investigating immersion liquid cooling (ILC) strategies for cold-start operation and their

interaction with lithium plating [22]. They demonstrated that maintaining batteries at elevated temperatures during fast charging using ILC reduced plating severity, while subsequent rapid cooling restored safe thermal conditions. Their modeling framework incorporated SEI growth and lithium plating, illustrating the delicate balance between thermal regulation and electrochemical side reactions. This study underscored the importance of coupling plating diagnostics with advanced cooling strategies, a perspective that aligns directly with the present work. Immersion cooling is a promising thermal management technique that significantly enhances lithium-ion battery performance and safety by submerging battery cells in a dielectric (nonconductive) fluid. This method involves submerging battery cells directly into a dielectric fluid, which offers superior heat dissipation compared to traditional cooling systems like air or indirect liquid cooling. Immersion cooling helps maintain a stable and uniform temperature distribution across all battery cells, preventing the formation of localized hotspots [23]. This uniformity is crucial for consistent performance and reliability of the battery pack. The use of immersion cooling addresses critical challenges associated with lithium-ion batteries, especially the generation of substantial heat during rapid charging and discharging processes [24].

Recent studies on Li-ion cell performance focus on predicting capacity fade, state of health, and cycle life with and without control of the thermal aspects. Multiple degradation mechanisms including SEI formation and lithium plating are associated with good or poor cycle life, and in some rare occasions, actual evidence of those phenomena is presented. The collective body of the literature related to lithium plating detection demonstrates significant progress through diverse methods ranging from voltage analysis, high precision coulometry, and impedance spectroscopy to mechanical pressure sensing and ultrasonic diagnostics. Many methods require specialized instrumentation, impose experimental interruptions, or lack the robustness needed for onboard BMS integration. Moreover, while thermal conditions are known to critically influence plating, few studies explicitly couple plating detection with advanced thermal management schemes such as immersion cooling.

The present study addressed the interplay between immersion cooling and lithium plating degradation by employing a comparative study. Experimental analysis was performed under both ambient conditions and immersed-cooled conditions to characterize and quantify lithium plating. A reference cell was aged via high rate cycling and subjected to a destructive physical analysis to confirm plating. In parallel, cells under immersion cooling were subjected to identical cycling and different flowrates, followed by EIS and pseudo-EIS measurements. The pseudo-EIS signatures from the immersed-cooled cells were correlated with the physically confirmed plating in the reference cell. The correlation enabled a nondestructive identification of lithium plating in the immersion-cooled cells, assessing how the thermal boundary conditions influence plating formation.

Methodology

Test Samples. Commercial LG M50T INR21700 cylindrical cells procured from a reputable vendor, with a graphite (C) anode and a lithium nickel manganese cobalt oxide cathode with a rated capacity of 5 Ah were used in this study. The cell was an energy cell with a maximum recommended charge and discharge rates of 0.7C-rate and 1.5C-rate, respectively. The nominal charge and discharge rates are 0.3C-rate and 0.2C-rate, respectively. The maximum continuous rate was used as a reference rate in the cycle life and lithium plating triggering conditions. The electrochemical tests were performed with an SBT0550 battery cycler (PEC Corporation). Cell temperatures were measured using K-type thermocouples.

Reference Test in Air. The first part of the study consisted of cycling a cell in air at 25 °C. The test was designed purposely to lead the cell into a lithium plating condition. EIS and pseudo-EIS were used to find any features, like a drop in the transition impedance, corroborating any possible presence of lithium plating within the cell. The EIS and pseudo-EIS results were published by, one of our research group members, Sarlashkar et al. [17]. Thermal aspects were not considered as part of the analysis, and no destructive physical analysis was performed on the plated cell.

Cycling tests included a sequence of pseudo-EIS followed by a static capacity (SC), hybrid pulse power characterization (HPPC), and cell cycling. The pseudo-EIS was performed at three different C-rates: 0.3C-rate, 0.5C-rate, and 0.7C-rate. Reference performance test (RPT) protocol was similar to the one presented here, and cycling was performed 2C constant current (CC) discharge down to 2.5 V, and a 1C CC charge up to 4.2 V with no rest for 20 cycles. The sequence was repeated 25 times until 500 cycles were completed. Preliminary EIS and pseudo-EIS were reported by Sarlashkar et al. and will not be discussed here [17].

Immersion Cooling Tests. The immersion cooling experiments were conducted using a custom-designed flow rig developed for a broader study on Li-ion battery thermal management [25]. The rig was designed to enable individual flow control for multiple cells while maintaining precise thermal and electrical isolation between them. Seven cylindrical cells were mounted within dedicated wells of a modular holder equipped with internal baffles to guide coolant flow uniformly across each cell surface. The coolant was circulated through a closed-loop system comprising a gear pump, inline heater, and plate heat exchanger to maintain a constant coolant inlet temperature of 25 °C. The flow direction was oriented perpendicular to the cell casing (cross-flow configuration) to achieve consistent heat transfer across the curved surface. Flow rates were varied systematically from 0 to 4 lpm to investigate the influence of convective boundary conditions on thermal and electrochemical behavior. Cell 1 (5159) was fully immersed under stagnant conditions (0 lpm), and cells 2–4 (5324, 5506, 5522) and cells 5–7 (5555, 5605, 5621) were tested at 2 lpm and 4 lpm, respectively.

Cycle life tests were performed on seven cells cycled under immersion cooling conditions with an inlet temperature of 25 °C. Cells were immersed in a common hydrocarbon-based coolant with appropriate low electrical conductivity and dielectric properties. All cells were cycled for 4 days followed by a 3-day RPT test. The short cycling test with frequent RPTs allowed for close monitoring of the state of health and detected the fast degradation caused by the fast-charge conditions. Eight RPTs and 70 cycles were performed on every cell.

Reference Performance Test and Pseudo-Electrochemical Impedance Spectroscopy. RPTs evaluated the battery performance parameters such as capacity, open-circuit-voltage, discharge and charge power capability, and internal resistance. Each RPT consisted of three main tests: discharge static capacity, HPPC, and pseudo-EIS, see Fig. 1(*a*). Both the SC and HPPC were carried out in accordance with the US DOE battery test manual for Plug-in Hybrid Electric Vehicles (PHEV) [26]. Salvi et al. analyzed SC and HPPC results and hence were out of the scope for this article [25]. Pseudo-EIS was performed using a modified version of the pseudo-EIS protocol proposed by Koleti that included a short discharge pulse to account for the discharge internal resistance.

Static capacity measured the cell capacity under the recommended manufacturer's nominal rate (C/5) at 25 °C. Capacity loss was normalized with respect to the SC from RPT0. HPPC provided information on the discharge internal resistance from 100% down to 0% SOC in 10% SOC increments. Cell SOC was adjusted using a C/2 discharge rate and rested for 1 h to ensure thermal and electrochemical equilibrium. HPPC at a given SOC was performed as follows: a 30-s discharge pulse at 0.6C, the maximum rate, was applied, followed by a 30-s rest. This was then followed by a

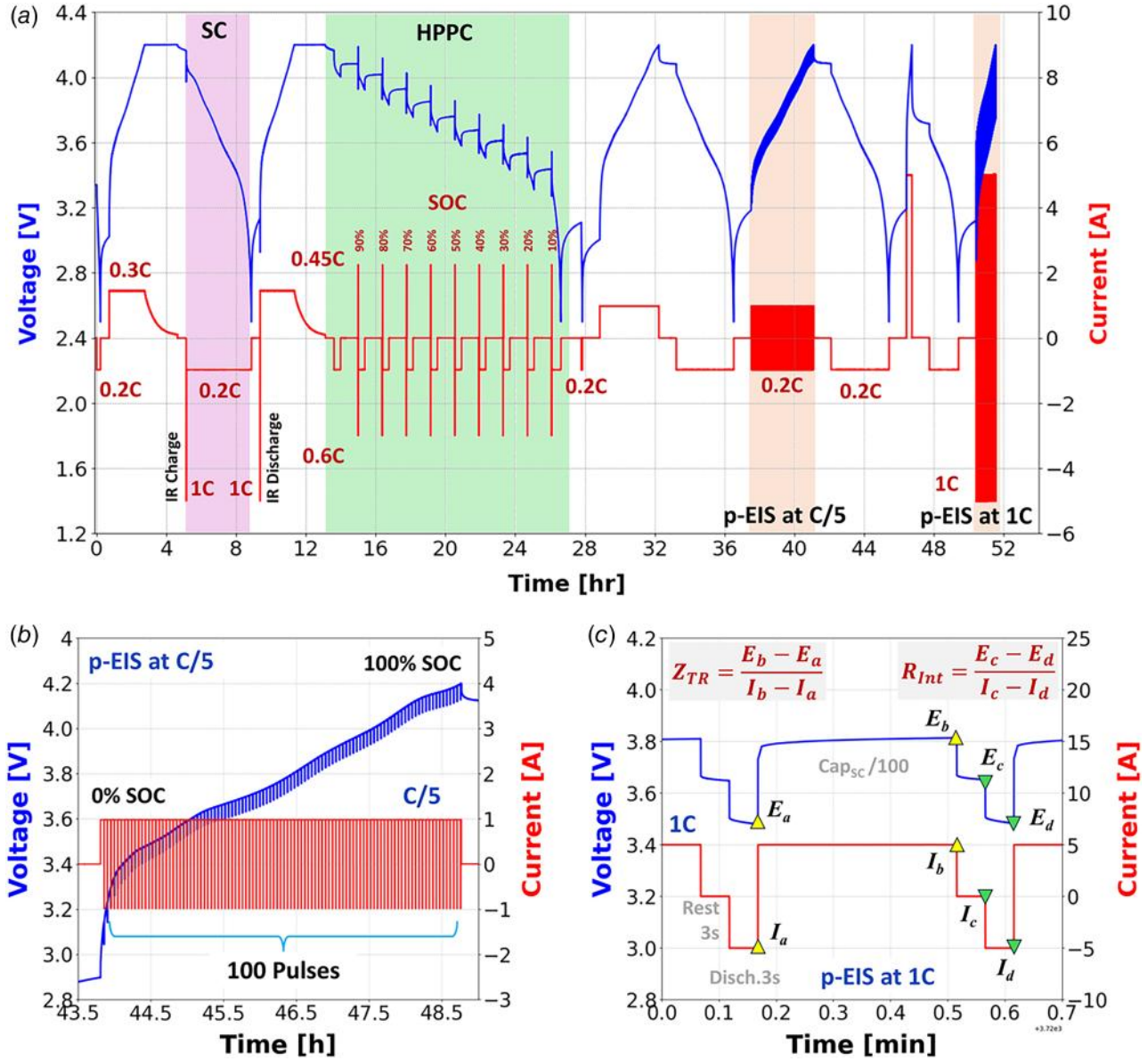

Fig. 1 Reference performance test: (*a*) full experimental test, (*b*) full pseudo-EIS test at C/5 rate, and (c) close up to pulses from pseudo-EIS test at 1C-rate

charge pulse at 0.45C (75% of a 0.6C discharge rate) and a 10-s rest.

The pseudo-EIS method emulated the EIS test by applying intermittent current pulses during charging. The purpose of these pulses was to capture the transition from charge transfer to diffusion in the impedance Nyquist plot. The transition frequency (f_{TR}) is the frequency where the knee between the charge transfer semicircle and the diffusion tail occurs. A key challenge was that the transition impedance (Z_{TR}) did not occur at a single, consistent frequency but varied with the state of charge. Once the transition frequency was identified, it was used to calculate a reference time ($1/f_{TR}$) for the diffusion phenomena. This reference time was consistent with the prior research, which suggested that it could range from 2 to 3 s [6], and it aligned with the time obtained from the current cell.

Therefore, the pseudo-EIS method was implemented in the battery cycler during the charging process from 0% to 100% SOC with pulses every 1% SOC. The charge capacity prior to pseudo-EIS was used as a reference for the SOC interval estimation. Roughly 100 pulses were applied while charging the cell, see Fig. 1(*b*). A charge current pulse (1C for high, 0.2C for low) was applied until the charge capacity exceeded 1/100th of the reference capacity to capture the charge transfer. The cell was then rested to allow lithium ions to diffuse into the graphite electrode. Based on the transition frequency analysis, a 3-s rest after the charge pulse was sufficient to capture both processes: charge transfer and diffusion. An additional 3-s discharge current pulse (1C for high, 0.2C for low) was also included to estimate the ohmic impedance value. The comparison between the charge and discharge pulses will show the relevance of high charge rate pulse in lithium plating detection.

Ageing Sequence. Prior to the cycling tests, all cells underwent a short beginning of life test under nominal test conditions. These data were used for clustering cells with similar charge and discharge capacities, internal resistance, and time constants. The clustering process is out of the scope of the article but mitigated possible cell-to-cell variation effects on the results. The cell nominal capacity was used as a reference for estimating charge and discharge rates. All cells were constant current, constant voltage charged at 1.3C-rate (6.5 A) up to 4.2 V with a cutoff

current of 100 mA (C/50). Then, cells were CC discharged at 0.2C-rate down to 2.5 V, with a 1-h rest period in between the charge and discharge steps.

Electrochemical Impedance Spectroscopy Test. Electrochemical impedance spectroscopy was performed along with the cycling at the beginning of life (BOL) and end of life (EOL). EIS tests were performed on the immersed cells at 0%, 50%, and 100% SOC using a Gamry 1010E potentiostat. Frequencies varied from 1 kHz down to 10 mHz with ten points per decade and an AC current excitation magnitude of 700 mA.

Destructive Physical Analysis. At the end of the cycle life testing in air, two cells were subjected to a destructive physical analysis aiming to confirm any presence of lithium plating. The postmortem analysis was performed on one cell aged in air (2632) and a fresh cell (2354). No cells aged under immerse cooling conditions were disassembled. The fresh cell served as a benchmark for comparing aged electrodes with pristine ones. The analysis included a detailed location of the zones with the presence of lithium plating. Prior to cell disassembly, the cells were discharged to 0% SOC. If the cell had presence of plated lithium, the discharge should not destroy that evidence. Additionally, the discharge was performed a few hours before the cell opening to prevent re-intercalation of lithium into the graphite phase [4]. Cells were disassembled in a Fisher Hamilton fume hood by following the procedure proposed by Juarez-Robles et al. [27].

Electrodes were harvested for physical inspection. Samples were harvested from the aged and fresh graphite anodes and analyzed using an optical microscope. Samples from the aged electrodes with evidence of plating were further analyzed using Raman spectroscopy to validate lithium plating presence.

Results and Discussion

Reference Cell Ageing in Air. The test sequence described earlier in the Methodology section is shown in Fig. 2. During the initial testing, RPTs included HPPC and SC and pseudo-EIS and were run using multiple programs. The results showed that pseudo-EIS took 2–3 days to fully run the three charging protocols

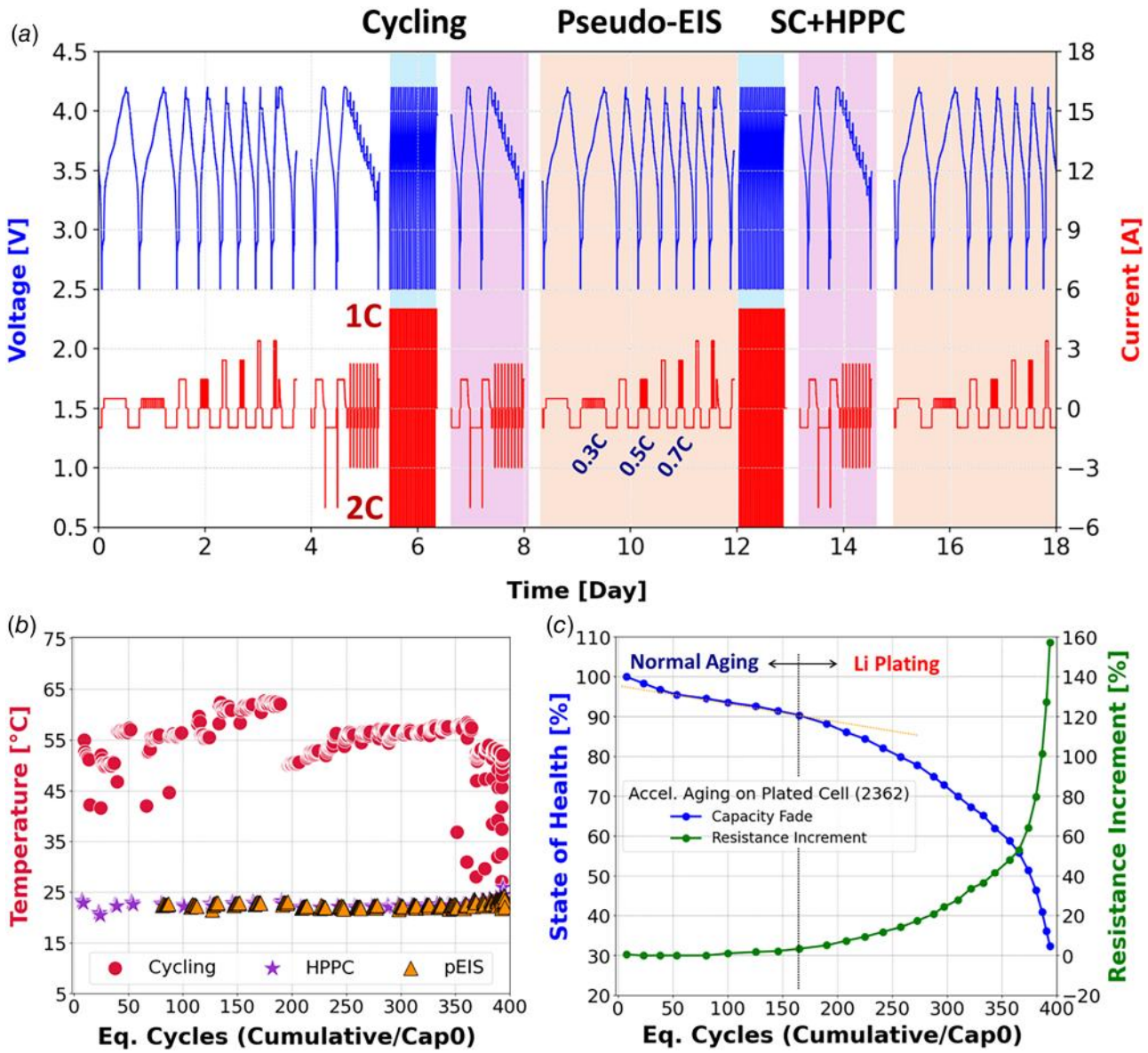

Fig. 2 Plated cell ageing results: (*a*) cycling sequence including pseudo-EIS, (*b*) max temperature, and (c) capacity fade and internal resistance increment

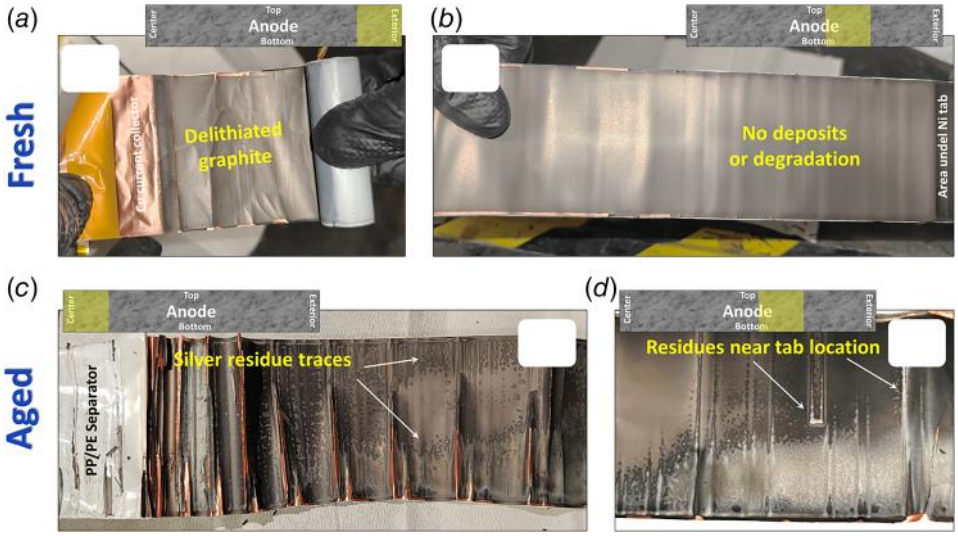

Fig. 3 Postmortem photos of fresh and aged graphite anodes. Fresh cell 2354: (*a*) electrode near the metal casing and (*b*) area near the internal nickel tab. Cycled aged cell 2632: (*c*) area near the central mandrel and (*d*) silver deposits below the nickel tab location.

with the intermittent pulses, see Fig. 2(*a*). Energy and capacity exchanged during pseudo-EIS and HPPC were also accounted for final Coulombic counting. The maximum temperature measured during the ageing tests is shown in Fig. 2(*b*). The HPPC and pseudo-EIS tests were performed at moderate and nominal rates, and hence, no significant temperature rise was observed. On the other hand, the ageing test was performed under an aggressive cycling condition. The high charge and discharge rates led to a temperature rise of 40 °C, especially in the middle of the life test. Around 200 equivalent cycles, capacity faded at a faster rate and internal resistance increased. At about 250 equivalent cycles, the cell reached the so-called end of life when the SOH dropped below 80%. The test continued until 500 regular cycles were complete.

At the end of the cycling test, the cell was at 32% SOH and resistance increased 159% relative to the initial value, Fig. 2(*c*). The cell went beyond the knee that separated the linear degradation and cell degradation due to lithium plating [6]. The knee appeared to happen between 150 and 200 equivalent cycles. The accelerated degradation rate trend coincided with a 10 °C maximum temperature reduction. The rapid capacity loss that followed the knee point significantly reduced the energy stored and consequently, the number of reactions happening during cycling. This reduction caused the heat generation to drop dramatically, a decrease so large that it overwhelmed the heat generation caused by the rising internal resistance. Consequently, the total heat generated beyond the 350 equivalent cycles decreased, resulting in the counterintuitive observation of a cooler cell despite its highly degraded and high-resistance state.

Destructive Physical Analysis. Cell 2362 was selected from the aforementioned test set with a state of health curve that exhibited a typical pattern of a cell with lithium plating presence. The EIS and pseudo-EIS analysis done by Sarlashkar et al. on this sample revealed a feasible presence of lithium plating [17]. The only missing part of the puzzle was showing actual evidence of plated lithium on the graphite anode.

The fresh cell 2354 was used as a reference for the pristine condition of the cell components and also subjected to destructive physical analysis. Any difference between the aged and fresh cells was caused by the high rate cycling test. The physical analysis of cathode, separators, and cell protections revealed no significant differences between the two cells. Although the separator did not have a protective alumina (Li_2O_3) layer, no dendrite formation within the separator was found. From here after, the analysis focused on the final condition of the graphite anode. Figure 3 shows the posttest pictures of the graphite electrodes. The gray color electrode surface shown in Fig. 3(*a*) indicated that the electrode was fully delithiated [28,29]. No deposits or marks on the electrode surface were observed to the naked eye. The black area on the fresh sample corresponded to the zone where the nickel tab internal current collector was connected, see Fig. 3(*b*). Conversely, the cycle aged anode exhibited a silver deposit on the top and bottom edges of the electrode and the area near the nickel tab, see Figs. 3(*c*) and 3(*d*). The metallic silver deposit was denser near the center of the cell, making the electrode flaky and causing detachment of the active particle from the current collector.

The silver color of the deposits confirmed the presence of a metallic solid on the electrode surface. Samples from each of the electrodes were taken to the optical microscope to validate the hypothesis that the metallic solid was in fact lithium metal. Figure 4 shows the micrographs taken at low and high magnification. Figures 4(*a*) and 4(*b*) show the pristine graphite active material. The high magnification micrograph showed a well-defined amorphous platelet shape. Figures 4(*c*) and 4(*d*) show the electrode surface of a sample harvested from the plated cell. The samples were purposely selected from an area on the electrode with the silver residue traces, see Fig. 3. The electrode morphology revealed an amorphous material covering the surface. The nature of the film can be graphite, SEI, Li metal, or a Li compound. The Raman spectrum of the Li metal has a peak at 1850 cm^{-1} [30]. The SEI band on the Raman spectra typically appears at ~500 cm^{-1} peak and ~1000 cm^{-1} peak, whereas lithiated graphite exhibits two peaks between 1000 and 1800 cm^{-1} [31]. The samples with Li deposits extracted from the plated cell 2362 reacted with oxygen and water when exposed to air. Raman spectra exhibited a 325 cm^{-1} and 364 cm^{-1} peaks, Fig. 4(*e*). The peaks were consistent with Li compounds like Li_2O, $LiOH{\cdot}H_2O$, or LiF, all of them with Raman shift below 500 cm^{-1} [30]. The physical and spectroscopic analyses confirmed the presence of lithium plating as one of the main degradation mechanism behind the capacity fade.

Ageing Results Under Immersion Cooling. Cycling tests in air at high rates led to lithium plating on the graphite anode while operating at high temperature. Now, the effect of immersion cooling on the cell ageing behavior was investigated along with the pseudo-EIS tool, which already proved its capability for detecting lithium plating.

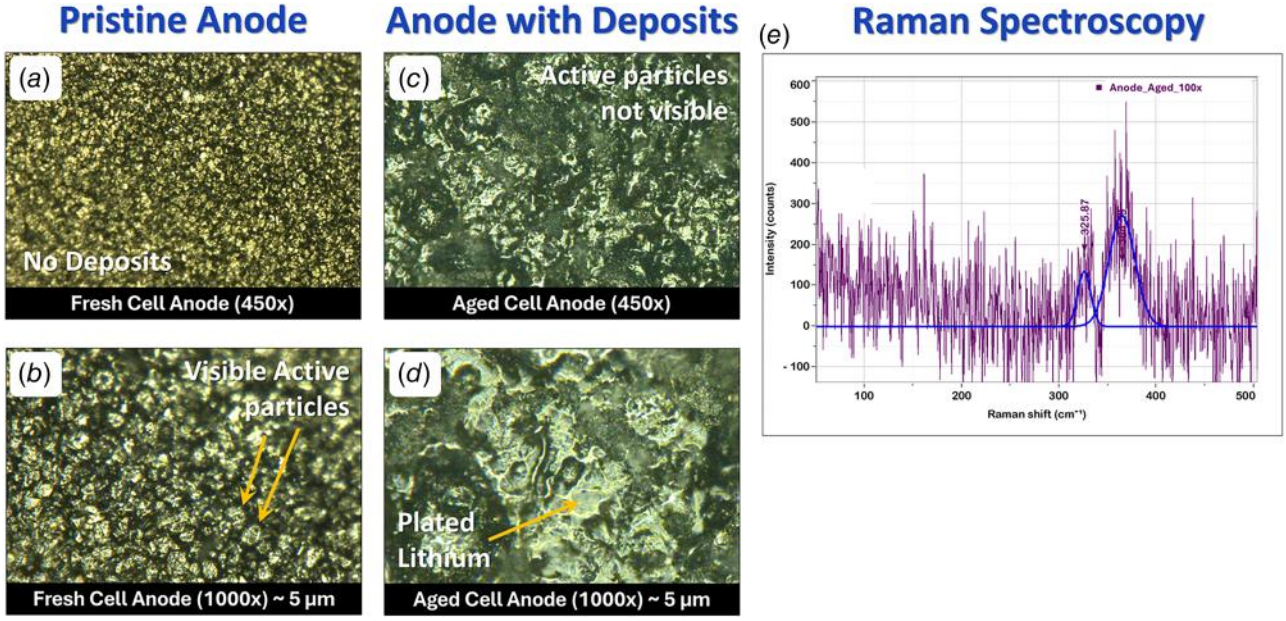

Fig. 4 Postmortem analysis of anode. Graphite sample harvested from a fresh cell 2354 at (*a*) 450× and (*b*) 1000× magnification. Graphite sample harvested from the lithium plated cell 2632 at (*c*) 450× and (*d*) 1000× magnification. (*e*) Raman spectra of plated graphite anode at 100×.

A representative full cycling test, using cell 5324 as example, is shown in Fig. 5(*a*). The high charge current can be identified as a large current peak. RPTs lasted for 3 days and cycling tests for 4 days. The short cycling test was purposely selected to monitor the cell SOH. RPTs provided a common platform to compare the performance of all seven cells. Figure 5(*b*) showed an accelerated capacity fade after only 70 equivalent cycles with a capacity reduction below the 80% SOH. In a real scenario, all cells would be considered to have reached their end of life since their SOH was lower than 80%, and they would not be considered eligible for a secondary application [32]. Counterintuitively, the cells immersed cooled with higher flowrates showed a higher capacity fade than its counterpart cooled with no flow (cell 5159). A high flowrate would increase the convective heat transfer coefficient and reduce the maximum cell temperature leading the cell to operate closer to the immersion coolant temperature. During cycling, at the BOL, the maximum temperature difference per cycle was 3.5 °C for the 0 lpm (cell 5159), 1.0–2.5 °C for the 2 lpm (cells 5324, 5506, 5522), and less than 1.0 °C for the 4 lpm (cells 5555, 5605, 5621), see Fig. 5(*d*). The temperature difference decreased in the high flowrate cells since the charge steps were getting shorter and shorter. Cell 5506 showed an increasing trend in temperature at EOL but that was due to a temperature increase on the coolant.

After 70 cycles, all immersed cells exhibited a nonlinear behavior with a knee around the 33-equivalent cycle. The knee seemed to happen earlier on the immerse cooled cells than the air cooled one. It is important to remark that cell 2632 tested in air was fast charged at 1C, whereas the immersed-cooled cells were charged at 1.3C. The electrochemical operation at high rates had a bigger impact on the cell ageing than the thermal conditions around the cell.

The cell internal resistance variation with cycling and temperature-controlled conditions revealed that the cell with zero flow showed the lowest increase in resistance, see Fig. 5(*c*), whereas the immersed-cooled cells with the 4 lpm coolant flowrate showed a faster degradation and highest internal resistance increase. Experimental results indicated that having a high flowrate increased the heat dissipation, reduced the cell temperature, increased cell resistance, and led to a faster degradation.

The battery internal resistance dependence is well known, and resistance decreases as the cell bulk temperature increases [33]. This is due to the accelerated electrochemical reactions, greater ionic conductivity, and enhanced ion transport and Li^+ diffusion within the battery [34]. Thus, a lower operating temperature would increase the internal resistance and cell overpotential, particularly at high charging rates and high SOCs, driving the anode potential below 0.0 V versus Li/Li^+ and leading to lithium plating and additional SEI formation. As the cell aged, the lithium plating degraded the cell and reduced lithium inventory but also lowered the internal resistance. The resistance reduction effect was previously reported by Zhang et al. [14]. Thus, the variation on resistance with cycling is a tradeoff between the cell operating temperature and the cumulative degradation mechanisms caused by charging the cell at high rates. Under air cooling conditions, high charging rates would cause an excessive heat generation contributing to capacity degradation and shorter cycle lifespan. Under immerse cooling conditions, the heat dissipation was already high, considering the low thermal mass of the cells. Adding a flow to the coolant increased the cooling effect more and dissipated most of the heat generated. This left any degradation effect due to high temperatures out of scope.

Electrochemical Impedance Spectroscopy Results and Transition Impedance. Electrochemical impedance spectroscopy was performed on the immersed cells at the BOL and EOL at 0%, 50%, and 100% SOC. Nyquist plots associated with cell impedance are shown in Fig. 6. Cell 5738 was a fresh cell included in the analysis as a reference to the BOL impedance conditions. Aged cells showed an increase in ohmic resistance (cross with x-axis at $-\mathrm{Im}(Z) = 0$) between 3 and 7 mΩ, no matter the SOC tested, with cell 5605 cooled at 4 lpm showing the largest increment. Charge transfer resistance, represented by the semicircle radius, increased as the cell aged for all SOCs due to thickening of SEI, morphology changes, and electrolyte decomposition. Interestingly, the 45 deg impedance tail associated with the diffusion process on the solid phase only showed an angle variation on the cell aged and cooled at 4 lpm at 100% SOC, see Fig. 6(*d*), which was the cell with the largest capacity fade. The angle change indicated that the ion diffusion through the electrode became sluggish due to pore clogging caused by either SEI thickening or lithium plating deposition.

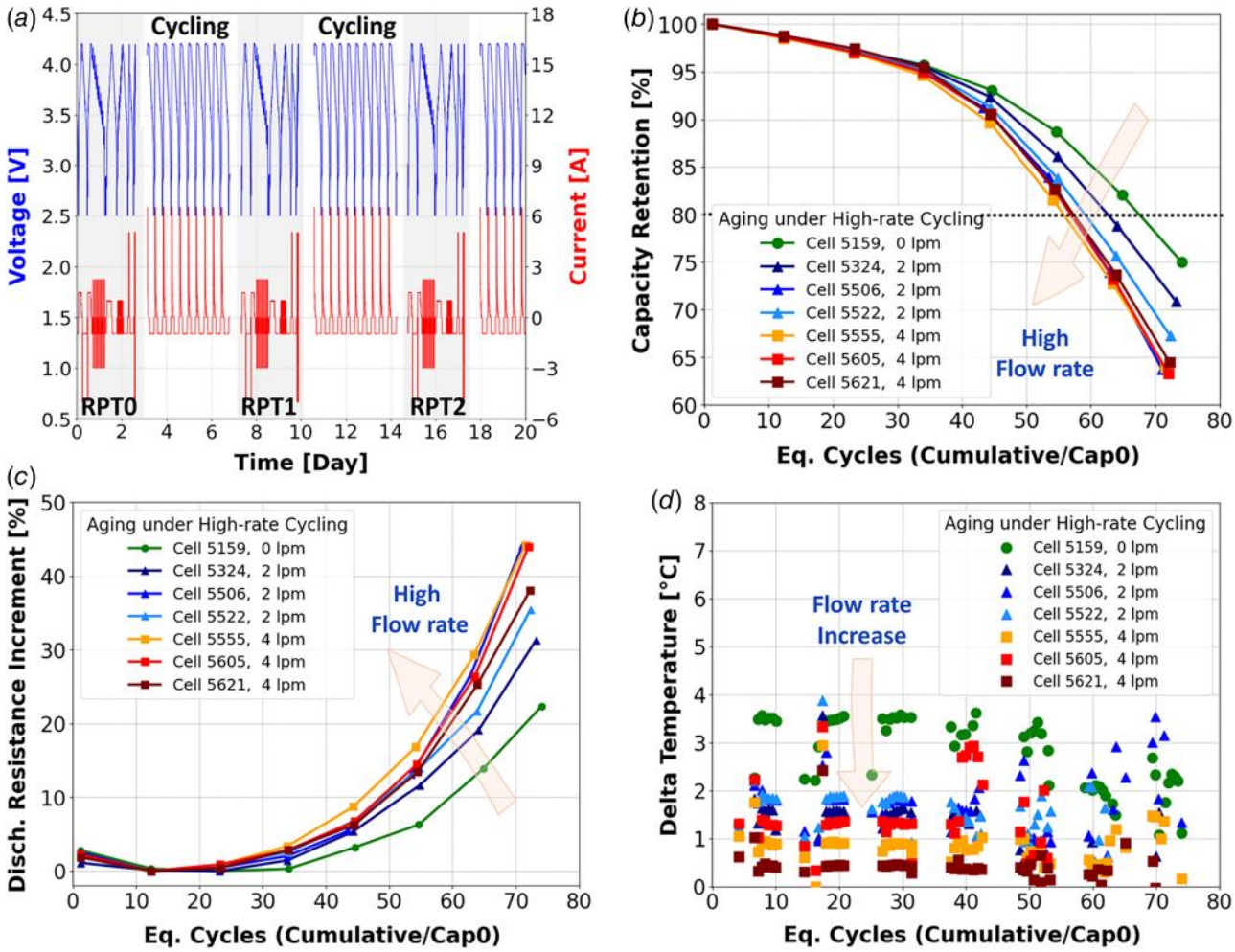

Fig. 5 Cycle ageing test. (*a*) Full test with RPTs and high rate cycling. State of health indicators: (*b*) static discharge capacity from RPTs and (*c*) internal resistance at the end of discharge. (*d*) Cell temperature increase.

Variation in the ohmic impedance, charge transfer, double-layer capacitance semicircles, and correlation to ageing degradation mechanisms had been well documented in the technical literature and were out of the scope for the current paper [33,35]. Instead, the analysis focused on the transition impedance, the knee represented by the markers shown in Fig. 6.

Implicit in the Nyquist plots of Fig. 6 was the frequency of the sinusoidal excitation applied by the EIS equipment. The frequency at which the transition between diffusion and charge transfer occurred and the magnitude of the transition impedance are key parameters and are plotted in Fig. 7. Note that the magnitude of the transition impedance, Fig. 7(*a*), as a group at various states of charge, increased with age, indicating inhibited transfer process resulting from pore clogging and tortuosity increase. Within each age group (BOL and EOL), the magnitude of impedance was larger under higher rates of coolant flow, indicating that the faster removal of heat exacerbated cell degradation. Thus, the higher the flowrate, the faster the cell degradation. The former statement applies only to charging under high rates but not necessarily to nominal cycling rates. Figure 7(*b*) shows the shift in frequency at which the transition occurs. Note that the frequency reduced with age, meaning that the characteristic timescale of the dynamic processes slowed down, indicating a reduction of lithium inventory as would be the case for lithium plating. The transition frequency was used as a reference for estimating the diffusion timescale, ranging from 50 ms to 2.2 s and agreeing with the values reported by Koleti et al. [16]. The diffusion timescale was the link between EIS and pseudo-EIS tests.

Pseudo-Electrochemical Impedance Spectroscopy. The pseudo-EIS protocol involved charging the cell to induce a charge transfer reaction, followed by a rest period that facilitated the diffusion of lithium ions into the graphite anode. Transition frequency analysis determined that a 3-s rest period was optimal, considering the 2.2 s timescale from diffusion, as it was sufficient to resolve both the high-frequency charge transfer process and the lower-frequency diffusion phenomena. This approach allowed for the efficient characterization of the cell's impedance response during the dynamic charging process.

The impedance measured during the pseudo-EIS protocol is shown in Fig. 8. Recall that the pseudo-EIS impedance is measured at low- and high-level current. Impedances at BOL were independent of the current level as seen in the lowermost traces in each subplot. The impedances measured at low- and high-level current show separation with age, with the high-current impedance being lower than the low-current impedance. This is consistent with the lowering of the transition frequency with age as noted in the regular EIS.

C-Rate Effect and Flowrate Effect. In previous sections, the battery SOH was evaluated in terms of Coulombic counting. Pseudo-EIS provided a different perspective of the ageing process. Figure 8 shows a comparison between the low- and high-level current responses. The low-level current (C/5, and C/10, thin solid lines) showed the characteristic high impedance near 0% and 100% SOC and lower impedance for intermediate values, with a bump in the middle most likely associated with a phase change

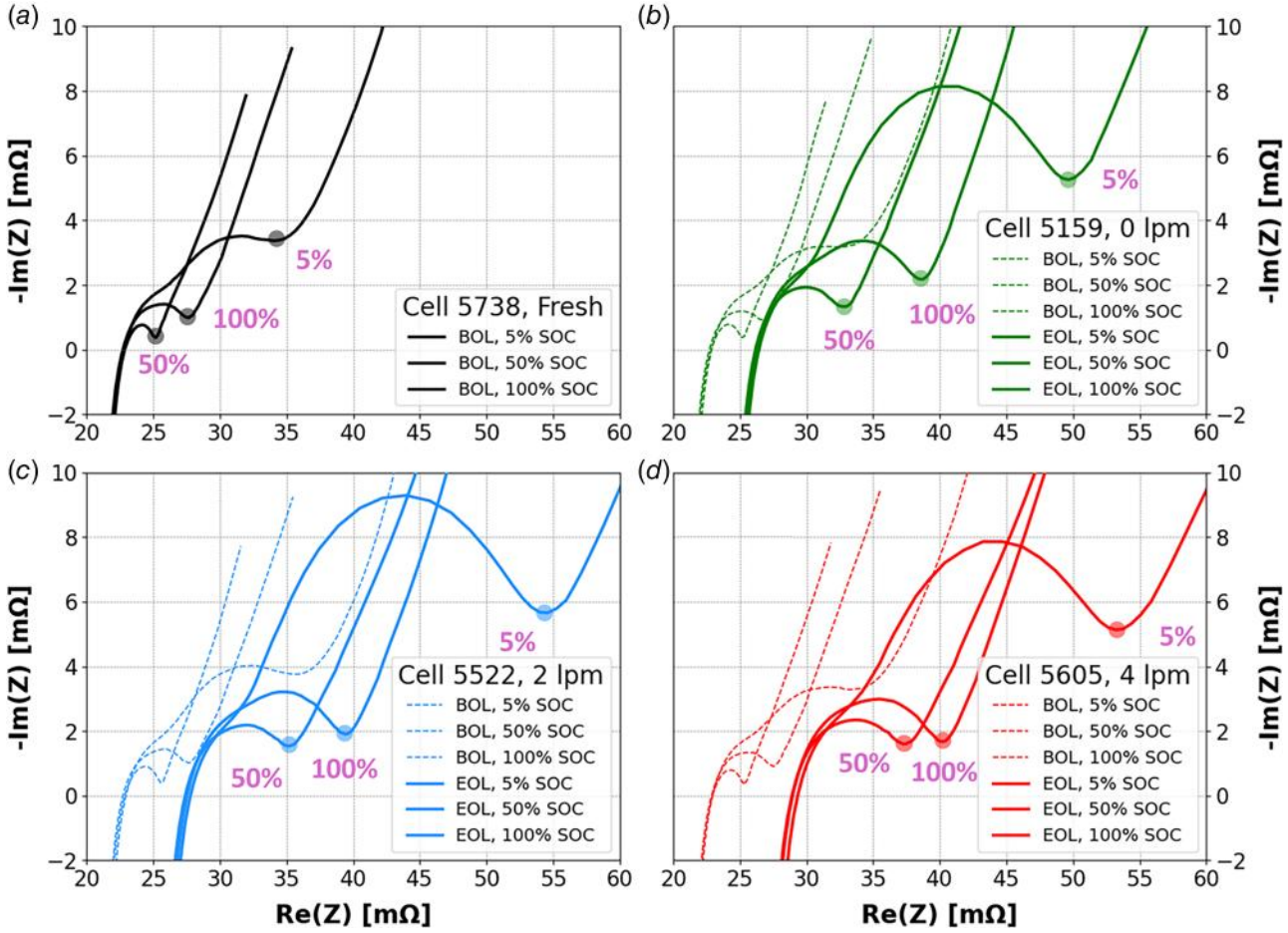

Fig. 6 EIS test results. Nyquist plots for (*a*) fresh cell 5738, (*b*) immersed cooled with no flow, 5159, (*c*) immersed with a 2 lpm flowrate, 5522, and (*d*) immersed with a 4 lpm flowrate, 5605.

in one of the electrodes. The transition impedance exhibited an initial agreement with the DC internal resistance trend [36]. The noisy behavior is associated with the weak response of the cell to a small current excitation. The four subplots in Fig. 8 include a transition impedance curve at the beginning, middle, and end of life. Despite the SOH represented by the cycle number or cooling condition, the low-level current curves always showed the same U-shape trend even at high SOC. The low current allowed the cell enough time to intercalate the ions exchanged during charge.

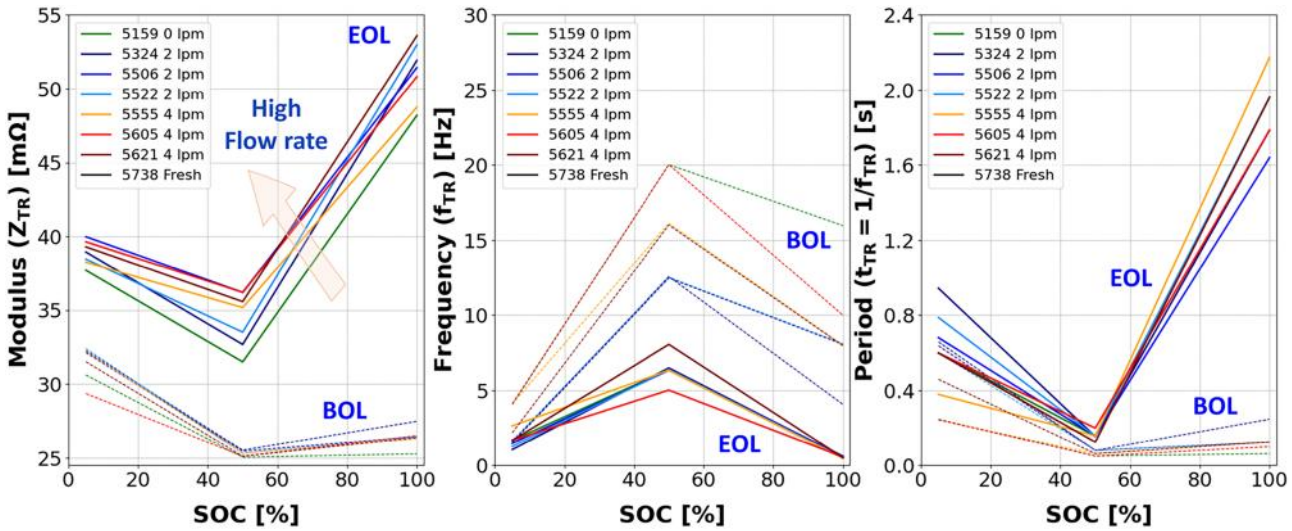

Fig. 7 EIS test results. Values for the transition knee between charge transfer semicircle and diffusion tail on the impedance Nyquist plots at 0%, 50%, and 100% SOC: (*a*) transition impedance, (*b*) transition frequency, and (*c*) period length associated to transition frequency.

Transition impedance for the high-level current curves (1C, thicker lines) from Fig. 8 showed a different trend. The first noticeable feature is the smoothness of the curves due to a clear response from the cell to the high-rate pulses. The second feature to highlight is the curve length shortening as the cell ages. The impedance increment led to larger polarization and the cell hitting V_{max} before fully charging the cell.

The cooling effect on ageing revealed that the cell aged in air had a longer cycle life (432 equivalent cycles at 1C) than the immerse cooled ones (~70 equivalent cycles at 1.3C) although a slightly lower charging rate was used. This implied that no thermal management control can be beneficial under high-rate conditions. Higher temperatures led to lower internal impedance and less incursions of the anode potential below 0.0 V versus Li/Li^+. The coolant flowrate played an additional decremental factor on ageing. High flowrates, 4 lpm, reduced cell capacity and increased transition impedance more than the cell immersed with no flow, see Figs. 8(*d*) and 8(*b*), respectively. The cell skin temperature difference between the 0 and 4 lpm cooling conditions was 2–3 °C. This small difference was enough to create a 10 mΩ difference at EOL.

Detection of plating was one of the main goals from this study. Pseudo-EIS at high-level rate for the reference cell showed an impedance drop at high SOC typically associated with lithium plating and later proved by physical inspection. The impedance drop signature analysis can be extended to the immersed-cooled cells. The shaded boxes in Fig. 8 highlighted the curve region where impedance drop might take place with the filled ones, indicating a confirmed or evident impedance drop. This signature became more evident at EOL and on the cells aged with high flowrates. A more detailed analysis of the ageing changes is presented in Fig. 9.

Cycle Life. Understanding the transition impedance evolution with ageing is important to identify impedance variations caused by the electrode phase transition and drop signature caused by lithium plating. Figure 9(*a*) shows the transition impedance at different SOH stages indicated by its equivalent cycle number on the left side. The curves had a natural bump (blue watermark arrow) at intermediate SOCs, associated with a phase transition. In the immersed-cooled cells, the bump shifted to the left due to the higher charge rate. This bump should not be confused with the lithium plating one, associated with a diffusion-limited condition and a reduction in impedance due to the presence of the Li metal.

Figure 9 shows the effect of the coolant flowrate on ageing. Figure 9(*a*) corresponds to air-cooled operation of the cell, while the remaining figures correspond to the higher C-rate and various flowrates of coolant. For the air-cooled cell, the impedance drop became evident after the equiv. cycle 142, see Fig. 9(*a*). This cycle is close to the capacity knee observed in Fig. 2(*b*), after which the accelerated degradation was observed. The impedance drop was less evident in cell 5159 immersed with no flow, see Fig. 9(*b*). This would indicate that the capacity loss observed in Fig. 5(*a*) might not necessarily have been driven by lithium plating. As the flowrate increased, the impedance drop became more predominant, particularly after cycle 50. The fast capacity loss observed in Fig. 5(*a*) for the 2 lpm and 4 lpm cells around cycle 50 agreed with the signature observed on the transition

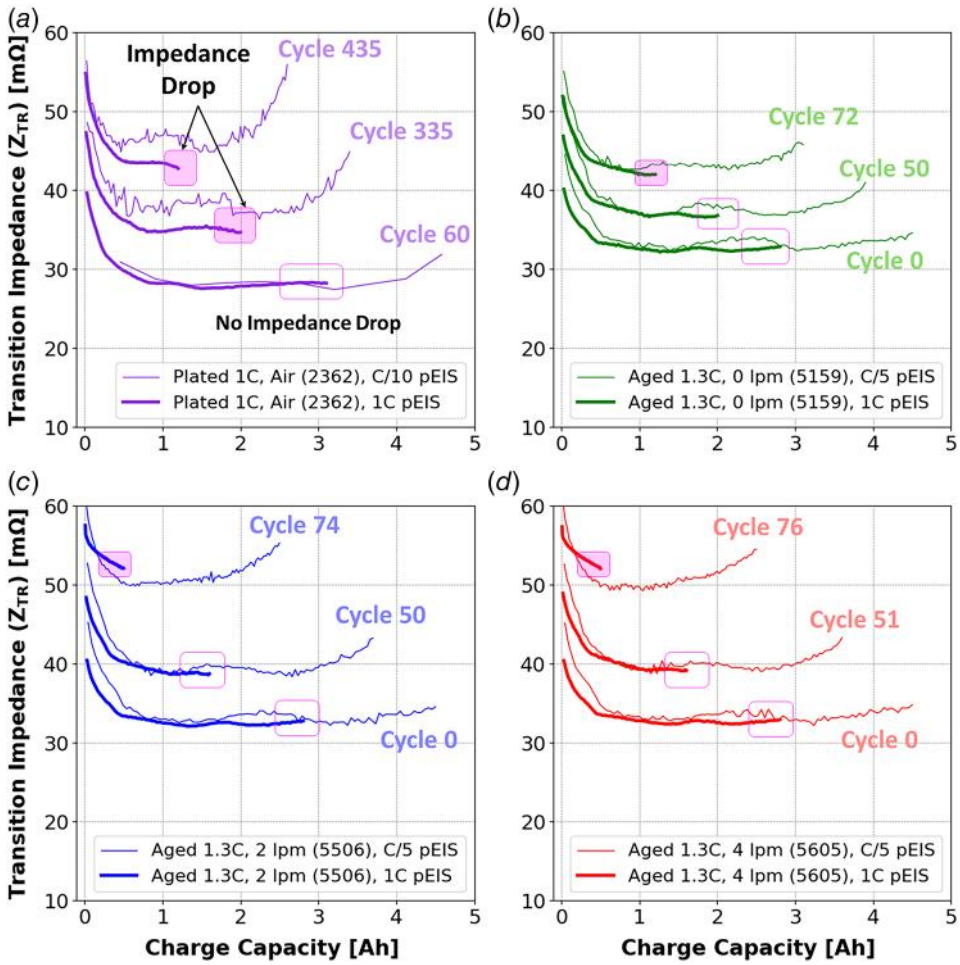

Fig. 8 Transition impedance variation at low- and high-rate trends: (*a*) reference cell in air; immersion with (*b*) 0 lpm, (*c*) 2 lpm, and (*d*) 4 lpm.

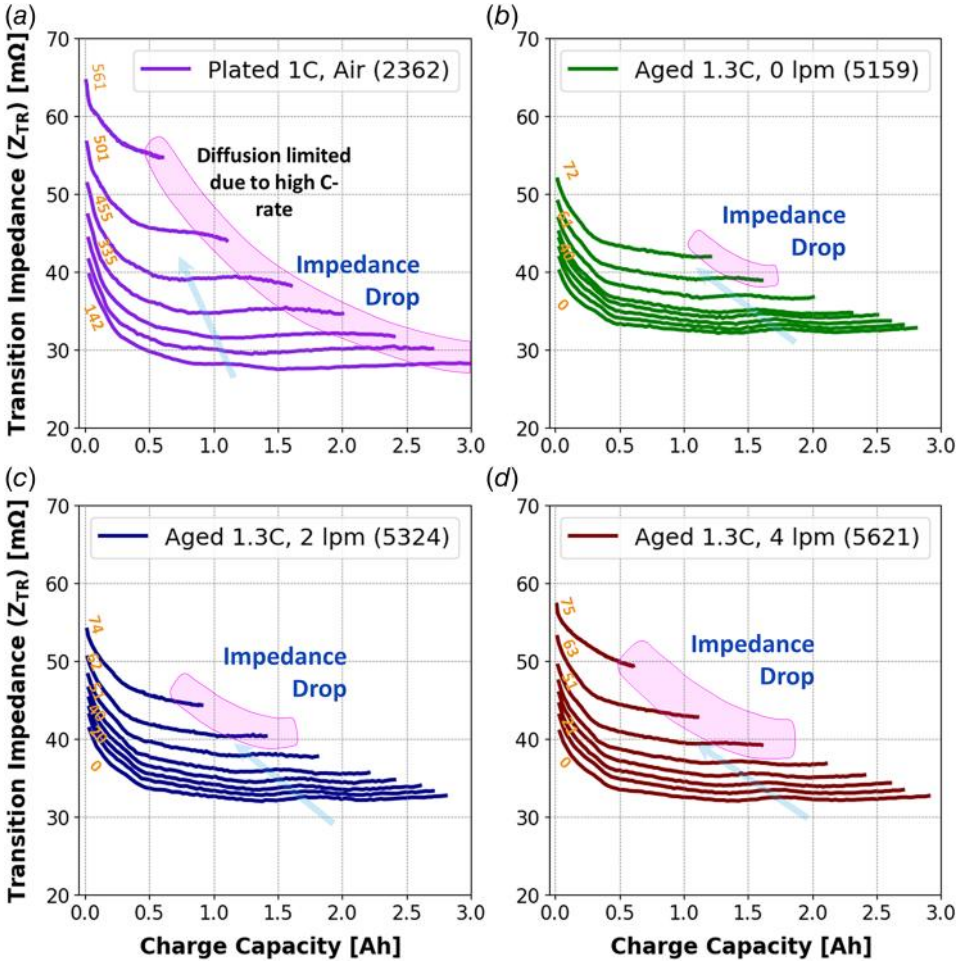

Fig. 9 Transition impedance variation with aging using high-rate pseudo-EIS. (*a*) Reference cell in air; immersion with (*b*) 0 lpm, (*c*) 2 lpm, and (*d*) 4 lpm. Note: Shaded areas indicate detected lithium plating.

impedance. These results revealed that higher flowrates were more detrimental to the cell, even more so with the higher rates of charging. As such, a battery management strategy can be derived from this observation, for instance, reducing or stopping the coolant flow under fast-charge conditions and restoring it for normal operation.

Conclusions

This study on immersed liquid cooling and its interaction with lithium plating was conducted in two parts. The first part involved ageing a lithium battery in air under conditions favorable to the formation of lithium plating. The cell was analyzed using the pseudo-EIS technique, and its ability to detect the presence of lithium plating was confirmed. The indicator for this phenomenon was a drop in the transition impedance at high SOC when the cell was charged under intermittent high-current pulses. The presence of plating within the cell was corroborated through the postmortem analysis. Once the validity of this technique as an indicator of SOH was proven, the effect of immersion cooling was analyzed.

In the second part of the study, seven cells were aged using high current while immersed in a dielectric cooling liquid. The goal was to investigate if thermal control could influence the battery's ageing tendency. Both no-flow and flow conditions were applied to the batteries. The results indicated that immersion cooling accelerated battery ageing, making them more susceptible to lithium plating formation. The higher the flowrate, the greater the battery capacity loss. The coolant temperature reduction increased the battery's impedance and induced greater lithium deposition. The cell aged in air performed better thanks to the heat generated during cycling. Evidence of lithium plating on the immersed cells was determined using pseudo-EIS with no need of the post-mortem analysis. Cells aged at high rate with a 4 lpm flowrate showed the characteristic impedance drop as the cell passed the capacity loss knee and aged more rapidly.

Utilizing the pseudo-EIS as a bridging technique, Li-plating was observed in both the air-cooled and immersion-cooled cell by tracking the transition impedance values as the cell ages. Aggressive heat transfer by immersion cooling and the associated well-controlled cell temperatures, in conjunction with high C-rates appeared to have had the unintended consequence of increasing discharge resistance and accelerating capacity fade. Any thermal ageing benefits were more than offset by the increased plating risk. A battery management strategy can be derived for fast charging, for example, reducing or stopping the coolant flow for charging and restoring it under normal operation.

Further analysis is needed to establish the relationship between cell degradation and cell age under nominal conditions, as well as the impact of higher fluid temperatures for the high C-rate immersion cooling test where the maximum temperature may approach that of the air-cooled reference test case.

Acknowledgment

The authors would like to acknowledge the technical contributions of Bapiraju Surampudi (deceased), Ian Smith, and Mickey Argo, Jr., for their work on conceptualization, testing, and analysis.

Funding Data

- The SwRI Electrified Vehicle and Energy Storage Evaluation (EVESE) consortium.

Conflict of Interest

There are no conflicts of interest.

Data Availability Statement

The authors attest that all data for this study are included in the paper.

References

[1] Juarez-Robles, D., Vyas, A. A., Fear, C., Jeevarajan, J. A., and Mukherjee, P. P., 2020, "Overcharge and Aging Analytics of Li-Ion Cells," J. Electrochem. Soc., **167**(9), p. 090547.
[2] Keil, P., and Jossen, A., 2016, "Charging Protocols for Lithium-Ion Batteries and Their Impact on Cycle Life—An Experimental Study With Different 18650 High-Power Cells," J. Energy Storage, **6**, pp. 125–141.
[3] Preger, Y., Barkholtz, H. M., Fresquez, A., Campbell, D. L., Juba, B. W., Romàn-Kustas, J., Ferreira, S. R., and Chalamala, B., 2020, "Degradation of Commercial Lithium-Ion Cells as a Function of Chemistry and Cycling Conditions," J. Electrochem. Soc., **167**(12), p. 120532.
[4] Fear, C., Adhikary, T., Carter, R., Mistry, A. N., Love, C. T., and Mukherjee, P. P., 2020, "In Operando Detection of the Onset and Mapping of Lithium Plating Regimes During Fast Charging of Lithium-Ion Batteries," ACS Appl. Mater. Interfaces, **12**(27), pp. 30438–30448.
[5] Tewari, D., and Mukherjee, P. P., 2019, "Mechanistic Understanding of Electrochemical Plating and Stripping of Metal Electrodes," J. Mater. Chem. A, **7**(9), pp. 4668–4688.
[6] Attia, P. M., Bills, A., Brosa Planella, F., Dechent, P., Dos Reis, G., Dubarry, M., Gasper, P., et al., 2022, "Review—'Knees' in Lithium-Ion Battery Aging Trajectories," J. Electrochem. Soc., **169**(6), p. 060517.
[7] Liu, Q., Du, C., Shen, B., Zuo, P., Cheng, X., Ma, Y., Yin, G., and Gao, Y., 2016, "Understanding Undesirable Anode Lithium Plating Issues in Lithium-Ion Batteries," RSC Adv., **6**(91), pp. 88683–88700.
[8] Janakiraman, U., Garrick, T. R., and Fortier, M. E., 2020, "Review—Lithium Plating Detection Methods in Li-Ion Batteries," J. Electrochem. Soc., **167**(16), p. 160552.
[9] Petzl, M., and Danzer, M. A., 2014, "Nondestructive Detection, Characterization, and Quantification of Lithium Plating in Commercial Lithium-Ion Batteries," J. Power Sources, **254**, pp. 80–87.
[10] Burns, J. C., Stevens, D. A., and Dahn, J. R., 2015, "In-Situ Detection of Lithium Plating Using High Precision Coulometry," J. Electrochem. Soc., **162**(6), pp. A959–A964.
[11] Chen, X., Li, L., Liu, M., Huang, T., and Yu, A., 2021, "Detection of Lithium Plating in Lithium-Ion Batteries by Distribution of Relaxation Times," J. Power Sources, **496**, pp. 1–9.
[12] Koseoglou, M., Tsioumas, E., Ferentinou, D., Jabbour, N., Papagiannis, D., and Mademlis, C., 2021, "Lithium Plating Detection Using Dynamic Electrochemical Impedance Spectroscopy in Lithium-Ion Batteries," J. Power Sources, **512**, pp. 1–10.
[13] Straßer, A., Adam, A., and Li, J., 2023, "In Operando Detection of Lithium Plating via Electrochemical Impedance Spectroscopy for Automotive Batteries," J. Power Sources, **580**, pp. 1–10.
[14] Zhang, X., Mao, S., Han, X., Cai, H., Zhu, Z., Li, S., Sun, Y., et al., 2025, "Online Lithium Plating Detection Based on Charging Internal Resistance for Lithium-Ion Batteries," J. Energy Storage, **108**, pp. 1–10.
[15] Shen, Y., Wang, X., Jiang, Z., Luo, B., Chen, D., Wei, X., and Dai, H., 2024, "Online Detection of Lithium Plating Onset During Constant and Multistage Constant Current Fast Charging for Lithium-Ion Batteries," Appl. Energy, **370**, pp. 1–14.
[16] Koleti, U. R., Dinh, T. Q., and Marco, J., 2020, "A New On-line Method for Lithium Plating Detection in Lithium-Ion Batteries," J. Power Sources, **451**, pp. 1–12.
[17] Sarlashkar, J. V., Surampudi, B., Chundru, V. R., and Downing, W. D., 2023, "Pseudo Electrochemical Impedance Spectroscopy Method for In-Situ Performance and Safety Assessment of Lithium-Ion Battery Energy Storage Systems for Grid-Scale Applications," 2023 IEEE International Systems Conference (SysCon), Vancouver, BC, Canada, Apr. 12–20, pp. 1–4.
[18] Huang, W., Ye, Y., Chen, H., Vila, R. A., Xiang, A., Wang, H., Liu, F., et al., 2022, "Onboard Early Detection and Mitigation of Lithium Plating in Fast-Charging Batteries," Nat. Commun., **13**(1), p. 7091.
[19] Zhu, Y., Yan, L., Han, S., Gu, M., Ma, S., Luo, Y., Meng, A., et al., 2025, "In Situ Lithium Plating Monitor for Lithium-Ion Batteries Enabled by Operando Pressure Detection," J. Power Sources, **631**, pp. 1–8.
[20] Xu, Z., Chen, X., Liu, S., Zhang, C., and Jiang, K., 2025, "Online Detection and In-Situ Characterization of Lithium Plating in Lithium-Ion Batteries Based on Ultrasonic Signals," J. Energy Storage, **116**, pp. 1–11.
[21] Ringbeck, F., Rahe, C., Fuchs, G., and Sauer, D. U., 2020, "Identification of Lithium Plating in Lithium-Ion Batteries by Electrical and Optical Methods," J. Electrochem. Soc., **167**(9), p. 090536.
[22] Liu, X., Li, Y., Gao, S., Zhou, Z., Wu, W.-T., Wei, L., Lyu, J., Li, Y., and Song, Y., 2025, "Efficient Cold-Starting Project With Mild Lithium Plating for Lithium-Ion Batteries Using Immersion Liquid Cooling at Low Temperatures," Appl. Energy, **384**, pp. 1–16.
[23] Salvi, S. S., Surampudi, B., Swarts, A., Sarlashkar, J., Smith, I., Alger, T., and Jain, A., 2024, "Experimental and Theoretical Analysis of Immersion Cooling of a Li-Ion Battery Module," ASME J. Electrochem. Energy Convers. Storage, **21**(4), p. 041001.
[24] Wahab, A., Najmi, A.-U.-H., Senobar, H., Amjady, N., Kemper, H., and Khayyam, H., 2025, "Immersion Cooling Innovations and Critical Hurdles in Li-Ion Battery Cooling for Future Electric Vehicles," Renewable Sustainable Energy Rev., **211**, pp. 1–24.
[25] Salvi, S. S., Swarts, A., and Juarez-Robles, D., 2025, "Impact of Immersion Cooling Variables in Li-Ion Battery Degradation: An Experimental Investigation," J. Energy Storage.
[26] Christophersen, J. P., 2014, "U.S. Department of Energy Vehicle Technologies Program: Battery Test Manual for Plug-In Hybrid Electric Vehicles," INL/EXT–14-32849, 1169249.
[27] Juarez-Robles, D., Jeevarajan, J. A., and Mukherjee, P. P., 2020, "Degradation-Safety Analytics in Lithium-Ion Cells: Part I. Aging Under Charge/Discharge Cycling," J. Electrochem. Soc., **167**(16), p. 160510.
[28] Manka, D., and Ivers-Tiffée, E., 2015, "Electro-Optical Measurements of Lithium Intercalation/De-Intercalation at Graphite Anode Surfaces," Electrochim. Acta, **186**, pp. 642–653.
[29] Hogrefe, C., Waldmann, T., Molinero, M. B., Wildner, L., Axmann, P., and Wohlfahrt-Mehrens, M., 2022, "Cross-Sectional In Situ Optical Microscopy With Simultaneous Electrochemical Measurements for Lithium-Ion Full Cells," J. Electrochem. Soc., **169**(5), p. 050519.
[30] Cabañero, M. A., Hagen, M., and Quiroga-González, E., 2021, "In-Operando Raman Study of Lithium Plating on Graphite Electrodes of Lithium Ion Batteries," Electrochim. Acta, **374**, pp. 1–9.
[31] Fonseca Rodrigues, M.-T., Maroni, V. A., Gosztola, D. J., Yao, K. P. C., Kalaga, K., Shkrob, I. A., and Abraham, D. P., 2019, "Lithium Acetylide: A Spectroscopic Marker for Lithium Deposition During Fast Charging of Li-Ion Cells," ACS Appl. Energy Mater., **2**(1), pp. 873–881.
[32] Fischer, M., Brand, M. J., Karger, A., Gomez, M. R., Rehm, M., Natterer, J., and Jossen, A., 2025, "How Degradation of Lithium-Ion Batteries Impacts Capacity Fade and Resistance Increase: A Systematic, Correlative Analysis," J. Power Sources, **656**, pp. 1–16.
[33] Barcellona, S., Colnago, S., Dotelli, G., Latorrata, S., and Piegari, L., 2022, "Aging Effect on the Variation of Li-Ion Battery Resistance as Function of Temperature and State of Charge," J. Energy Storage, **50**, pp. 1–12.
[34] Belgibayeva, A., Rakhmetova, A., Rakhatkyzy, M., Kairova, M., Mukushev, I., Issatayev, N., Kalimuldina, G., Nurpeissova, A., Sun, Y.-K., and Bakenov, Z., 2023, "Lithium-Ion Batteries for Low-Temperature Applications: Limiting Factors and Solutions," J. Power Sources, **557**, pp. 1–18.
[35] Li, M., Xu, W., Zhang, S., Liu, L., Hussain, A., Hu, E., Zhang, J., Mao, Z., and Chen, Z., 2025, "State of Health Estimation and Battery Management: A Review of Health Indicators, Models and Machine Learning," Materials, **18**(1), p. 145.
[36] Chen, L., Zhang, M., Ding, Y., Wu, S., Li, Y., Liang, G., Li, H., and Pan, H., 2021, "Estimation the Internal Resistance of Lithium-Ion-Battery Using a Multi-Factor Dynamic Internal Resistance Model With an Error Compensation Strategy," Energy Rep., **7**, pp. 3050–3059.